ADVANCED HEALTHCARE MATERIALS

www.advhealthmat.de

Multimodal Cancer Theranosis Using Hyaluronate-Conjugated Molybdenum Disulfide

Myeong-Hwan Shin, Eun-Yeong Park, Seulgi Han, Ho Sang Jung, Do Hee Keum, Geon-Hui Lee, Taeyeon Kim, Chulhong Kim, Ki Su Kim, Seok Hyun Yun, and Sei Kwang Hahn**

Among various 2D nanomaterials, molybdenum disulfide (MoS_2) exhibits unique visible photoluminescence with high absorption at the near-infrared (NIR) range. Despite these optical properties, the efforts to use MoS_2 nanomaterials for optical imaging and photothermal therapy are hampered by their instability and low intracellular delivery efficiency. Multifunctional MoS_2 conjugated with hyaluronate (HA) for cancer theranosis is reported herein. HA facilitates the delivery of MoS_2 to tumor cells by the HA-receptor mediated endocytosis. In BALB/c nude mice inoculated with a colorectal cancer cell line of HCT116, HA-MoS_2 conjugates appear to be accumulated in the primary tumor at a content more than that in the liver and kidney. The disulfide bonding between MoS_2 and thiolated HA seems to degrade in the cytoplasm, releasing MoS_2 sheets in stacks and enhancing luminescence efficiency. The HA-MoS_2 conjugates are readily detected via photoacoustic imaging as well as upconversion and downconversion fluorescence imaging. With NIR light illumination, HA-MoS_2 conjugates enable highly effective photothermal tumor ablation. All these results confirm the promising potential of HA-MoS_2 conjugates for cancer theranosis.

1. Introduction

A variety of nanomaterials have been widely investigated for theranostic applications including iron oxide nanoparticles (IONPs),[1] gold nanoparticles (AuNPs),[2] silica nanoparticles (SiNPs),[3] upconversion nanoparticles (UCNPs),[4] polymeric nanoparticles,[5] and emerging 2D nanomaterials.[6–8] Molybdenum disulfide (MoS_2), one of the 2D graphene analogues, has unique optical properties when exfoliated to nanoscale monolayers. Its crystal structure consists of 0.65 nm thick layer of Mo atoms with two adjacent sulfide atomic layers stacked by van der Waals force.[9] This material was reported to have indirect to direct semiconductor transition when exfoliated from bulk to monolayer, resulting in extremely enhanced photoluminescence (PL) for light sensing, light harvesting, and light emitting.[10] MoS_2 was reported to have 7.8 times higher near- infrared (NIR) absorbance than graphene oxide with its extinction coefficient of 29.2 $L \cdot mol^{-1} \cdot cm^{-1}$ at 800 nm, which is much higher than that of gold nanorods.[11] In addition, MoS_2 has been reported to have unsaturated d-orbitals,[12] chemically active edge defect,[9] and sulfur vacancy[13] as a target site for introducing functional ligands. Accordingly, MoS_2 nanomaterials have been extensively investigated as an NIR absorbing agent for various biomedical applications.[14–16] Despite these unique properties, biomedical applications of MoS_2 have been limited due to the low serum stability and inefficient intracellular delivery.[17,18] To mitigate these problems, MoS_2 was surface-modified with biocompatible and nontoxic organic materials such as poly(ethylene glycol) (PEG), chitosan (CS), polyaniline (PANI), and polypyrrole (PPy).[18–22]

Here, we developed HA-MoS_2 conjugate for cancer theranosis with bimodal imaging of fluorescence microscopy

M.-H. Shin, S. Han, H. S. Jung, D. H. Keum, G.-H. Lee, T. Kim, Prof. S. K. Hahn
Department of Materials Science and Engineering
Pohang University of Science and Technology (POSTECH)
77 Cheongam-ro, Nam-gu, Pohang, Gyeongbuk 37673, Republic of Korea
E-mail: skhanb@postech.ac.kr

E.-Y. Park, Prof. C. Kim
Department of Electrical Engineering
Pohang University of Science and Technology (POSTECH)
77 Cheongam-ro, Nam-gu, Pohang, Gyeongbuk 37673, Republic of Korea

Prof. C. Kim, Prof. S. K. Hahn
Department of Creative IT Engineering
Pohang University of Science and Technology (POSTECH)
77 Cheongam-ro, Nam-gu, Pohang, Gyeongbuk 37673, Republic of Korea

Prof. K. S. Kim
Department of Organic Materials Science and Engineering
College of Engineering
Pusan National University
2 Busandaehak-ro 63 beon-gil, Geumjeong-gu, Busan 46241, Republic of Korea
E-mail: kisukim@pusan.ac.kr

Prof. K. S. Kim, Prof. S. K. Hahn
PHI BIOMED Co.
#613, 12 Gangnam-daero 65-gil, Seocho-gu, Seoul 06612, Republic of Korea

Prof. K. S. Kim, Prof. S. H. Yun
Wellman Center for Photomedicine
Harvard Medical School and Massachusetts General Hospital
65 Landsdowne St. UP-5, Cambridge, MA 02139, USA

DOI: 10.1002/adhm.201801036

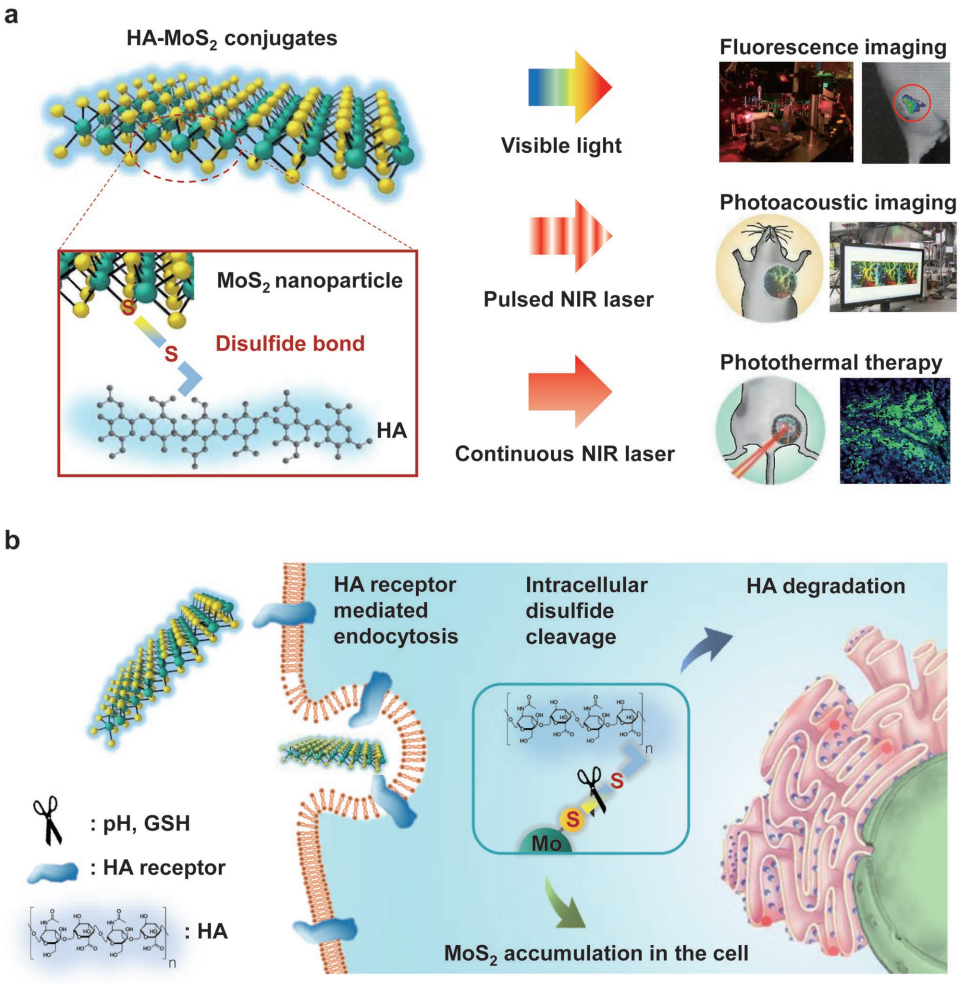

Figure 1. Schematic illustration of theranostic HA-MoS_2 conjugates. a) Multifunctional HA-MoS_2 conjugates for multimodal cancer theranosis using different light sources. b) Target-specific delivery of HA-MoS_2 conjugates to tumor cells via HA receptor–mediated endocytosis and its intracellular disulfide cleavage in the reducing environment.

and photoacoustic tomography (PAT), and target-specific photothermal therapy (PTT) (**Figure 1**). HA is one of the best natural biopolymers and has been widely used for target-specific drug delivery via HA receptors such as cluster determinant 44 (CD44), hyaluronan receptor for endocytosis (HARE), and lymphatic vessel endothelial hyaluronan receptor-1 (LYVE-1) usually over-expressed on various tumor cells.[23,24] As shown in Figure 1b, HA-MoS_2 conjugate prepared by facile disulfide bond formation between MoS_2 and thiolated HA (HA-SH) can bind to the HA receptors over-expressed on tumor cells. After cellular uptake by the HA receptor-mediated endocytosis, the disulfide bond of HA-MoS_2 conjugate can be cleaved in the cytoplasm due to the reducing environment of low pH and glutathione (GSH) during the endosomal escape.[25] While HA naturally degrades by hyaluronidases of Hyal-1 and Hyal-2,[26] the following aggregation of unstable MoS_2 nanoparticle in the cytoplasm can contribute to enhance the optical signal and the photothermal effect in the tumor cells for effective cancer theranosis.

2. Results and Discussion

2.1. Preparation and Characterization of HA-MoS_2 Conjugates

MoS_2 nanoparticle was simply prepared by the solvothermal and exfoliation process.[27] Bulk MoS_2 powder was dispersed in 1-methy-2-pyrrolidinone (NMP) following the probe-sonication. After keeping at 140 °C with vigorous stirring, the brownish yellow MoS_2 nanoparticle could be collected by centrifugation and dialysis against deionized (DI) water. HA was chemically modified with cystamine to introduce thiol groups, which was attached to the MoS_2 surface via disulfide bond formation. Atomic force microscope (AFM) analysis clearly showed the monolayer morphologies of both MoS_2 nanomaterials and HA-MoS_2 conjugates (**Figure 2**a). Transmission electron microscope (TEM) was used to analyze the morphology and the particle size of MoS_2 and HA-MoS_2 conjugates (Figure 2b). The lateral size was increased after HA conjugation due to the surface wrapping of MoS_2 nanoparticle with HA.[28] The individual MoS_2 nanomaterials had a mean particle size of 61.9 nm

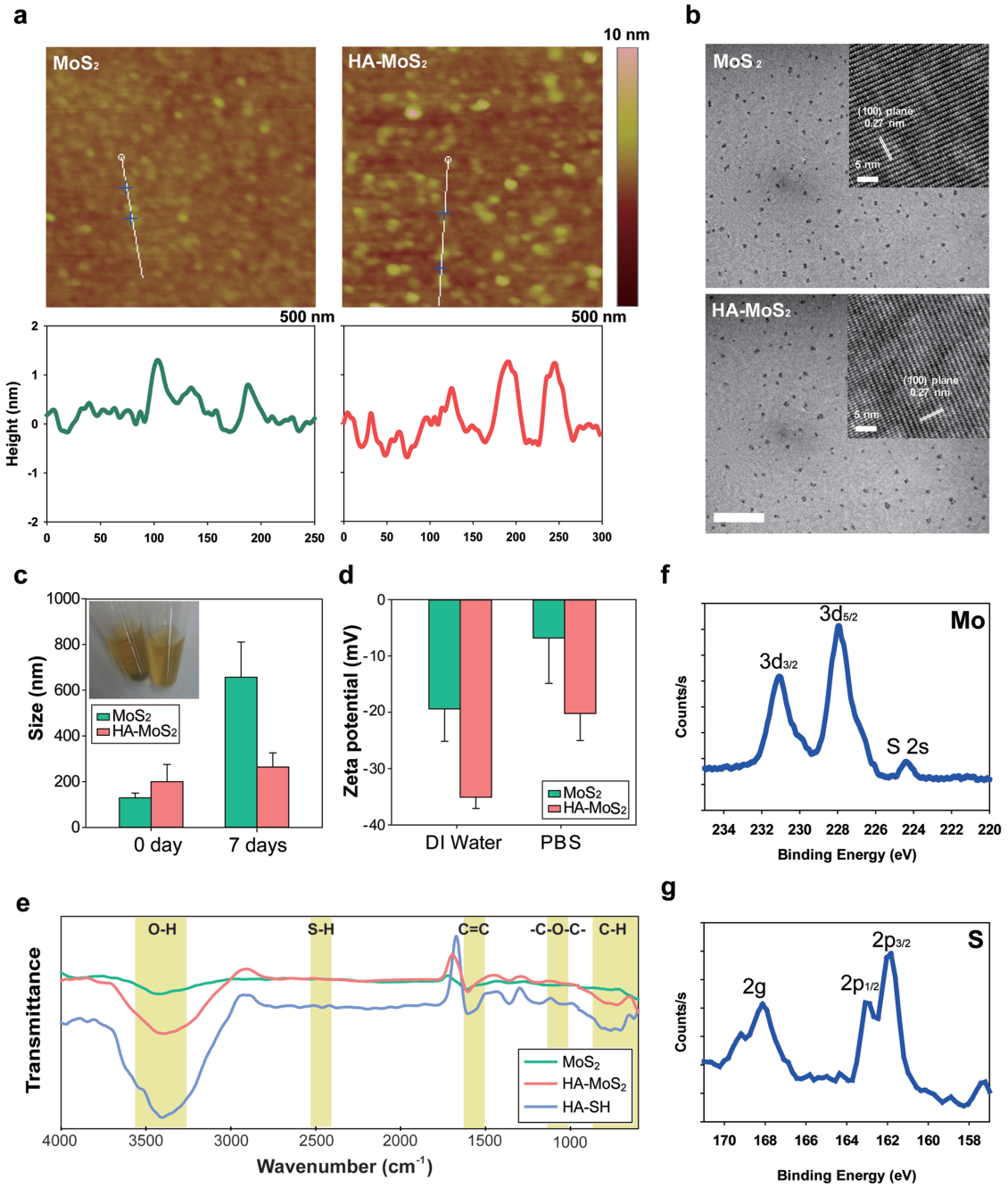

Figure 2. Characterization of HA-MoS_2 conjugates. a) AFM images of MoS_2 (left) and HA-MoS_2 conjugates (right). b) TEM images of MoS_2 (upper) and HA-MoS_2 conjugates (bottom) (scale bar = 500 nm). (inset) HR-TEM images of MoS_2 and HA-MoS_2 conjugates, respectively. c) The hydrodynamic size of MoS_2 and HA-MoS_2 conjugates dissolved in PBS at day 0 (129 ± 21.2 and 129 ± 21.2 nm, respectively) and day 7 (657 ± 153.4 and 264 ± 62.11 nm, respectively). (inset) A photo-image of MoS_2 (left) and HA-MoS_2 (right) after 7 days in PBS. d) The Zeta-potential of MoS_2 and HA-MoS_2 conjugates in DI water or PBS. e) FT-IR spectra of MoS_2, HA-SH, and HA-MoS_2 conjugates. f) Mo 3d and g) S 2p XPS analysis of HA-MoS_2 conjugates.

with 0.615 nm of thickness corresponding to the thickness of monolayer of MoS_2. Both the size and thickness of HA-MoS_2 conjugates were slightly increased to 85.9 and 1.10 nm, respectively. In addition, high-resolution TEM (HR-TEM) was performed to observe the crystal structure. The inset of Figure 2b shows the uniform (100) plane of each sample.

According to the dynamic light scattering (DLS) analysis, the hydrodynamic size of MoS_2 nanoparticle was ≈129 ± 21.2 nm in phosphate buffer saline (PBS) and the size of HA-MoS_2 conjugate was ≈200 ± 75.31 nm (Figure 2c), which were well matched with the results from TEM and AFM. After 7 days, however, the particle size of MoS_2 increased to ≈657 ± 153.4 nm due to the aggregation and stacking, whereas that of HA-MoS_2 conjugate only slightly increased to ≈264 ± 62.11 nm without aggregation (see the inset of Figure 2c and Figure S1, Supporting Information). After conjugation of MoS_2 with HA, the Zeta

potential was changed from −19.4 ± 5.76 to −35.1 ± 1.98 mV in DI water and from −6.8 ± 8.08 to −20.2 ± 4.81 mV in PBS, respectively (Figure 2d). These results revealed the better stability of HA-MoS_2 conjugates than that of MoS_2 nanomaterials in the physiological condition.

Fourier transform-infrared spectroscopy (FT-IR) analysis showed the dominant HA peaks from HA-MoS_2 conjugates. The peak of HA-SH was diminished after conjugation to MoS_2 nanoparticle with thiol S-H stretch (2500 cm^{-1}), carboxylic acid O–H stretch (3400 cm^{-1}), C=C stretch (1650 cm^{-1}), ether –C–O–C– (1100 cm^{-1}), and alkene sp^2 C–H bend at 1000 cm^{-1} (Figure 2e). Especially, the peak of S-H disappeared reflecting the disulfide bond formation. In addition, X-ray photoelectron spectroscopy (XPS) of HA-MoS_2 conjugate showed the covalent functionalization between HA-SH and MoS_2 nanomaterials. The atomic ratio of Mo to S increased from 1:2 to 1:6.67 after conjugation of MoS_2 nanoparticle with HA-SH.[29] The binding energy peak of Mo $3d_{5/2}$ and Mo $3d_{3/2}$ appeared at 232.6 and 229.4 eV, whereas that of S $2p_{3/2}$ and S $2p_{1/2}$ appeared at 163.0 and 161.8 eV, respectively. In comparison with the previous report on XPS analysis of MoS_2, both Mo 3d and S 2p peaks showed no significant change after conjugation with HA. In other words, HA did not change the innate 2H structure of MoS_2.[9] Additionally, the large oxidation peak of S 2p was observed at 168.1 eV, corresponding to the sulfate of HA by the exposure to ambient condition (Figure 2f,g).[30] Raman spectroscopy of HA-MoS_2 conjugates also showed similar pattern with the previously reported monolayer MoS_2.[27] E_{2g} (384 cm^{-1}) and A_{1g} (408 cm^{-1}) peaks were detected in Figure S2 in the Supporting Information. All these results confirmed the successful synthesis of monolayer MoS_2 and functionalization of HA onto MoS_2 nanoparticle, showing better physiological stability.

2.2. Optical Properties of HA-MoS_2 Conjugates

Figure 3a shows UV–vis spectroscopy of MoS_2 nanosheets exhibiting two absorption (excitation) bands at 610 and 654 nm. These bands might correspond to the direct transition at κ point by spin-orbit coupling of valence band.[31] The excitation bands were diminished after sonicating nanosheets to nanoparticles as reported elsewhere.[24] The PL of both MoS_2 and HA-MoS_2 conjugates was also analyzed under UV light illumination (Figure 3b). The peak of PL intensity at each wavelength was shifted to a longer wavelength with increasing excitation wavelength. Remarkably, we could observe upconversion fluorescence of HA-MoS_2 conjugates by excitation at the NIR region (Figure 3c). The upconverted PL intensity was relatively lower than that of downconversion fluorescence. The upconversion emission wavelength of HA-MoS_2 conjugates (525 nm) was not changed after excitation at various wavelengths from 650 to 800 nm, showing the stronger PL intensity at the higher NIR wavelength. This extraordinary optical property might be ascribed to anti-Stokes PL at the κ point where the direct exciton transition occurs.[32] These unique optical properties of MoS_2 were hardly affected by HA modification like other wrapping polymers on the MoS_2 surface as reported elsewhere.[30,31] On the basis of these results, we carried out confocal microscopy of HA-MoS_2 conjugates uptaken into HCT116 cells at various excitation wavelengths (Figure 3d). We could observe multicolor fluorescence of blue, green, yellow, and red from the cells at different wavelength. There were some spots with exceptionally strong PL intensity in the cytoplasm due to the aggregation of MoS_2 nanomaterials in the cells, whereas they were not observed in the bright field image (Figure 3e).

In addition, MoS_2 showed excellent photoacoustic (PA) characteristics. Figure 3f shows PA signals by converting pulsed NIR laser into ultrasonic emission. The PA signals of both MoS_2 and HA-MoS_2 conjugates decreased with increasing wavelength. MoS_2 without HA conjugation showed higher signals in all range of wavelength than HA-MoS_2 conjugates, likely due to the thermal vibration broadening of HA chain. The heat generated by NIR laser illumination might diffuse from MoS_2 to HA chain by heat transport, which might diminish the PA signals.[33] To assess the photothermal property of HA-MoS_2 conjugates, the temperature of HA-MoS_2 conjugate solution was measured at various concentrations of HA-MoS_2 conjugates under continuous NIR laser illumination. Owing to the efficient light-to-heat conversion of HA-MoS_2 conjugates, the solution temperature was increased with increasing NIR exposure times and conjugate concentrations. At a concentration of 200 μg mL^{-1}, the solution temperature increased more than 25 °C by NIR laser illumination for 10 min. This temperature increase over 43 °C was regarded enough for photothermal ablation of cancer cells (Figure 3g).[28] Figure S3 in Supporting Information showed the photothermal conversion efficiency and the photothermal stability of HA-MoS_2 conjugates. The photothermal conversion efficiency of HA-MoS_2 conjugates was calculated to be 11.5%, which was slightly lower than that of PEG-MoS_2 (27.6%) and MoS_2-CS (24.4%).[15,18] The lower photothermal conversion efficiency of HA-MoS_2 conjugates might be ascribed to the smaller particle size and the higher PL at the NIR region than those of MoS_2 nanoflakes in the PEG-MoS_2 and MoS_2-CS of the previous reports.

2.3. In Situ Disulfide Cleavage after HA Receptor–Mediated Endocytosis

The effect of HA conjugation was assessed on the physiological stability of MoS_2 nanomaterials, which is the most important characteristic for all nanoplatforms used in circulating systems.[34] The conjugation of MoS_2 with HA could prevent the stacking of MoS_2 nanomaterials by electrostatic repulsion between HA chains, making the conjugates stable. Since exocytosis frequently occurs in case of stable nanoparticles, the aggregation of nanoparticles in the cytoplasm can prevent their exocytosis with the increased size.[35] In addition, the nanoparticle aggregation can cause the redshift of absorption wavelength, resulting in high phothothermal efficiency for the NIR laser.[33] To take advantages of these characteristics, we assessed the cleavage of disulfide bonding in HA-MoS_2 conjugates and the resulting aggregation in the intracellular reducing environment with glutathione and low pH.[25]

In order for that, HA-MoS_2 conjugates were treated with tris(2-carboxyethyl)phosphine (TCEP) as a reducing agent in PBS. According to DLS analysis (**Figure 4**a), the hydrodynamic size increased from 329.8 ± 66.95 to 404.9 ± 64.71 nm at 24 h

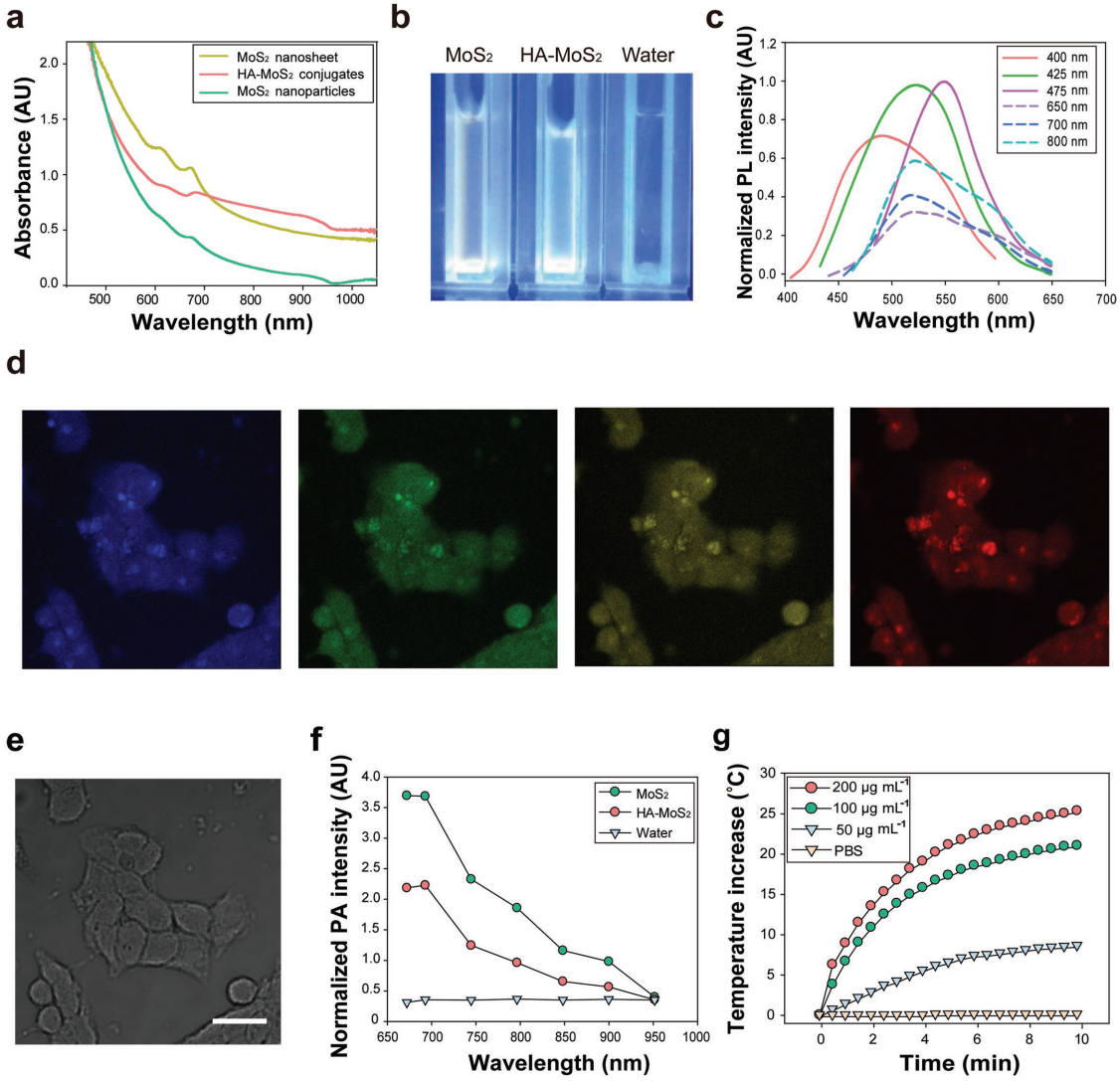

Figure 3. Optical properties of HA-MoS_2 conjugates and in vitro multicolor cell images. a) UV–vis absorption spectra of HA-MoS_2 conjugates, MoS_2 nanoparticle, and MoS_2 nanosheet. b) A photo-image of MoS_2 (left), HA-MoS_2 (middle), and DI water (right) under UV illumination. c) Both upconversion and downconversion PL of HA-MoS_2 conjugates depending on its excitation wavelength. Confocal microscopic image of HCT116 cells incubated with HA-MoS_2 conjugates at the excitation wavelength of d) 446, 570, 612, and 653 nm (from left) in comparison with e) bright field image (scale bar = 10 μm). f) Normalized PA intensity of MoS_2 and HA-MoS_2 conjugates in the NIR region. g) Photothermal effect of HA-MoS_2 conjugates at various concentrations.

posttreatment of TCEP. The HA-MoS_2 conjugates were well dispersed in PBS, but MoS_2 nanomaterials cleaved from HA-MoS_2 conjugates were aggregated in PBS after TCEP treatment (see the inset of Figure 4a). The surface charge was also changed from −17.85 ± 13.1 to −6.77 ± 8.82 mV, which was similar with the value of MoS_2 in PBS (Figures 2d and 4b). These results revealed the full cleavage of HA-MoS_2 conjugates by TCEP and the aggregation of MoS_2 nanomaterials. In addition, the change of photothermal effect was assessed before and after cleavage of disulfide bonding. In the presence of TCEP, the photothermal effect was slightly enhanced due to the aggregation of MoS_2 (Figure 4c). The aggregates of MoS_2 nanomaterials after disulfide bond cleavage showed higher NIR absorbing property than that of HA-MoS_2 conjugates which might be attributed to the size-dependent optical extinction coefficient change of nanoparticles.[36–38]

After that, we carried out in vitro confocal microscopy to observe the disulfide bond cleavage in the cytoplasm (Figure 4d,e). After incubation of HCT116 cells (human colon carcinoma) with Hilyte647-labeled HA-MoS_2 conjugates for 5 min, the fluorescence of both HA (red) and MoS_2 (green) appeared to be merged in the cytoplasm (Figure 4d). However, after incubation for 24 h, the fluorescence was separated to red (HA) and green (MoS_2), reflecting the apparent cleavage of disulfide bonding between HA and MoS_2 (Figure 4e). In addition, we could observe some green aggregates in the cells, which were in accordance with some big fluorescence spots observed in Figure 3d. From in vitro bioimaging results in Figures 3 and 4, we could confirm the feasibility of HA-MoS_2 conjugates as a bimodal imaging contrast agent for both fluorescence and PA imaging.

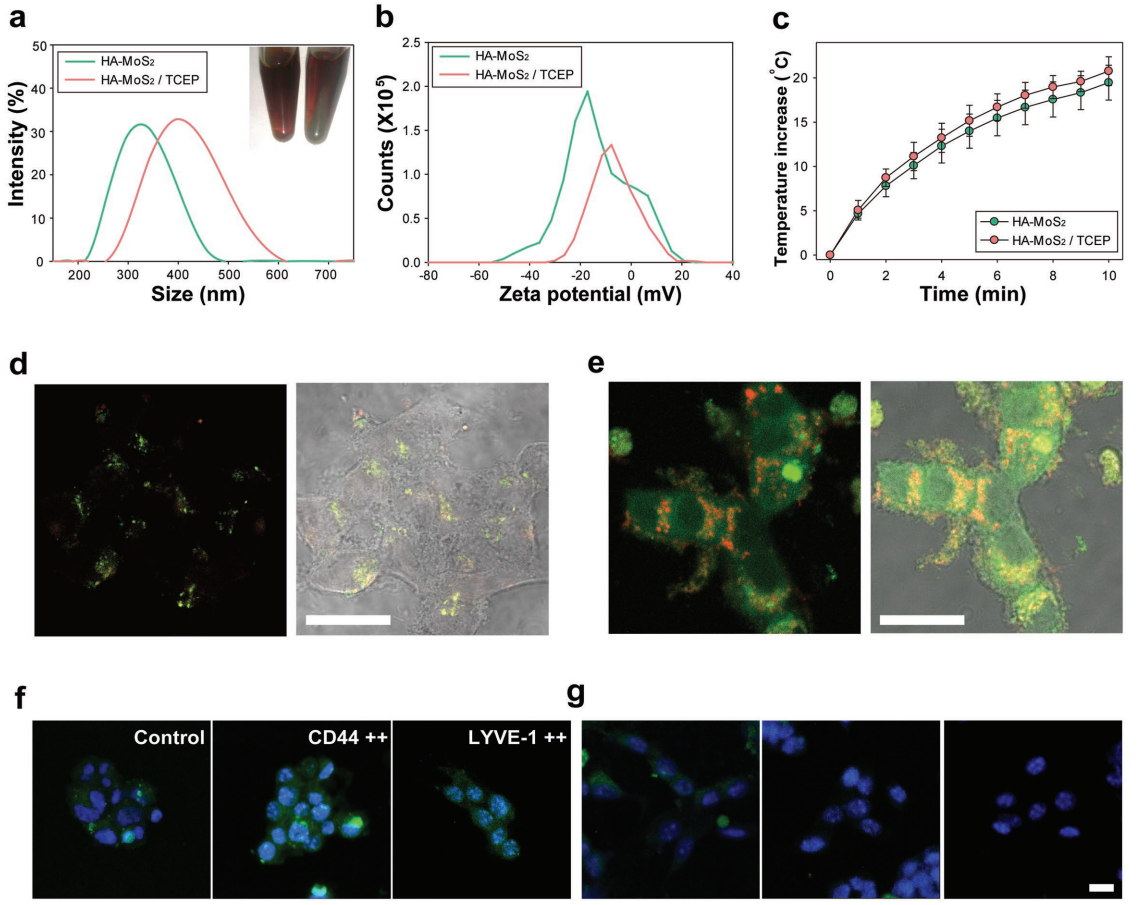

Figure 4. Effect of intracellular disulfide cleavage and HA-mediated endocytosis. DLS analysis for a) the hydrodynamic diameter change from 329.8 ± 66.95 to 404.9 ± 64.71 nm and b) the Zeta-potential change of HA-MoS_2 conjugates from −17.85 ± 13.1 to −6.77 ± 8.82 mV after treatment with TCEP as a reducing agent. (inset) A photo-image of HA-MoS_2 conjugates after treatment without (left) and with (right) TCEP, and the following centrifugation. c) The solution temperature change of HA-MoS_2 conjugates under NIR illumination without and with TCEP treatment. Confocal microscopic images of dye-labeled HA-MoS_2 conjugates in HCT116 cells after incubation for d) 5 min and e) 24 h (scale bar = 25 µm). Confocal microscopic imaging of HA-MoS_2 treated HEK293 (left), HCT116 (middle), and B16F10 (right) cells f) without and g) with HA preincubation (scale bar = 10 µm).

Before in vivo experiments, we carried out confocal imaging to assess the HA receptor–mediated endocytosis of HA-MoS_2 conjugates in HCT116 and B16F10 cells with highly expressed HA receptors and HEK293 cells without HA receptors after preincubation with an excess amount of HA.[23,24,28] Figure 4f,g shows the effect of HA preincubation on the HA receptor–mediated endocytosis. As clearly shown, the uptake of HA-MoS_2 conjugates was significantly reduced due to the competitive binding of HA in the HCT116 and B16F10 cells, whereas only slight change was observed in the HEK293 cells. These results confirmed the target-specific delivery of HA-MoS_2 conjugates via the HA receptor–mediated endocytosis.

2.4. In Vivo Bioimaging of HA-MoS_2 Conjugates

We carried out in vivo bioimaging of HA-MoS_2 conjugates in the tumor animal model of BALB/c nude mice inoculated with HCT116 cells. IVIS fluorescence imaging was performed after both subcutaneous (*sc*) and intravenous (*iv*) injections of HA-MoS_2 conjugates. We could observe the fluorescence signal of HA-MoS_2 conjugates at the injection site and confirm the feasibility of HA-MoS_2 conjugates for fluorescence bioimaging applications (**Figure 5**a). After that, we further performed ex vivo bioimaging of PBS, PEG-MoS_2 conjugates as a control and HA-MoS_2 conjugates to investigate the tumor-targeting affinity and the whole body biodistribution (Figure 5b). The fluorescence intensity was quantified in the region of interest (ROI) of dissected organs including lung, liver, kidney, spleen, and tumor (Figure 5c). Since the fluorescence intensity of HA-MoS_2 conjugate was significantly higher than that of PEG-MoS_2 conjugates ($^{**}p < 0.01$) in the tumor, we could confirm the effective target-specific delivery of HA-MoS_2 conjugates to the tumor. Remarkably, HA-MoS_2 conjugates appeared to accumulate in the primary tumor more than in the liver and kidney 24 h post-injection. The results might be caused by the HA receptor–mediated endocytosis with enhanced permeation of HA-MoS_2 conjugates and retention in the forms of the stacked MoS_2 within the cancer cells.[39,40]

Next, PA maximum amplitude projection (MAP) imaging of HA-MoS_2 conjugates was performed in tumor-bearing mice using an acoustic-resolution reflection mode PA imaging system at the wavelength of 680 and 850 nm for up to 4 h (Figure 5d–g).

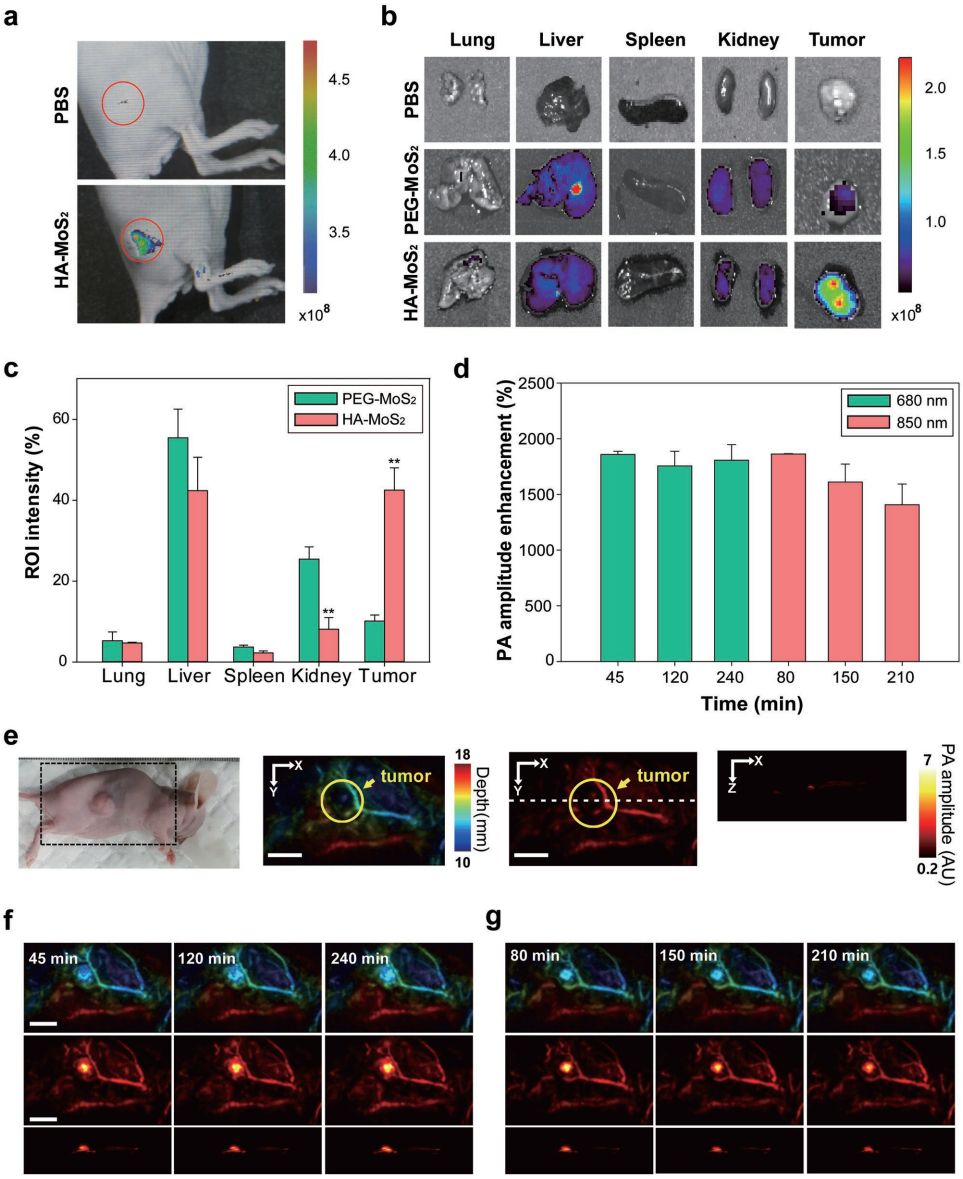

Figure 5. In vivo fluorescence and PA imaging of HA-MoS_2 conjugates. a) IVIS imaging of PBS and HA-MoS_2 conjugates after intradermal injection into the tumor (red circle) region. b) Ex vivo imaging of dissected lungs, livers, kidneys, spleens, and tumors after tail-veil injections of PBS, PEG-MoS_2, and HA-MoS_2 conjugates. c) Quantitative fluorescence analysis of PEG-MoS_2 and HA-MoS_2 conjugates in the organs for the assessment of tumor targeting affinity (**$p < 0.01$, PEG-MoS_2 vs HA-MoS_2 conjugates). d) The PA amplitude enhancement of HA-MoS_2 conjugates compared to the control (PBS) image at both 680 and 850 nm wavelengths with the depth profile of the highest signals for 240 min. e) A photo-image and PA MAP image of mouse in respect to depth (left) and amplitude (right) before injection of HA-MoS_2 conjugates. The PA signals at 30 and 240 min after intratumoral injection of HA-MoS_2 conjugates at f) 680 and g) 850 nm wavelengths in respect to depth (upper) and intensity (bottom).

The data showed 1860 folds higher enhancement of PA signals in average compared to the control at both wavelengths 1 h post-injection. Previously, traditional PA agents showed several hundred percent increase of PA signals after local injection.[41,42] The results might be explained by the extremely high light-to-heat conversion efficiency of HA-MoS_2 conjugates. The PA amplitudes at both wavelengths were maintained even after 4 h, especially at the wavelength of 680 nm (Figure 5d), in contrast to other organic PA agents with a short residence time.[43,44] While there was no PA signal on the tumor before injection (Figure 5e), the PA signal of HA-MoS_2 conjugates was clearly shown at the tumor site after intratumoral injection of HA-MoS_2 conjugates (Figure 5f,g). From all these results, we could confirm the potential of HA-MoS_2 conjugates as a bimodal imaging contrast agent for in vivo fluorescence and PA imaging.

2.5. In Vivo Photothermal Cancer Therapy Using HA-MoS_2 Conjugates

Before in vivo therapeutic applications, we investigated the photothermal effect of HA-MoS_2 conjugates in HCT116 cells at

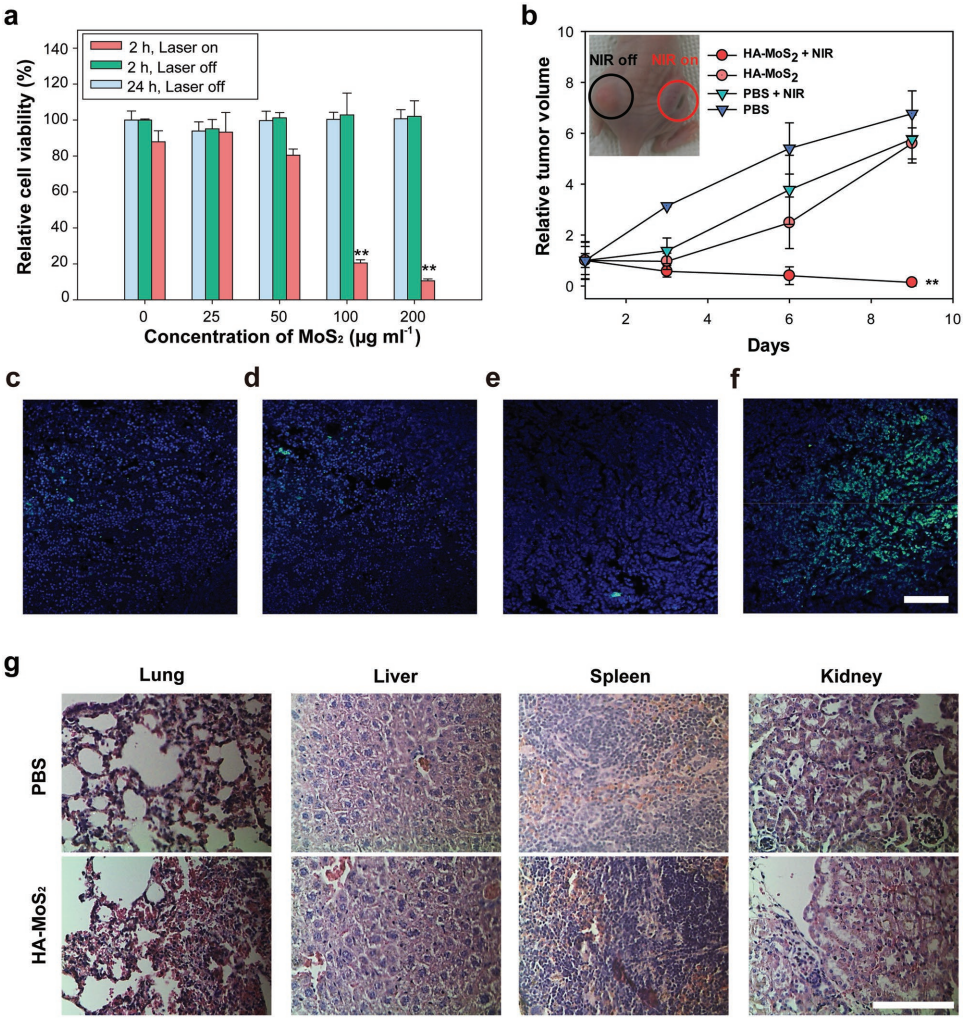

Figure 6. In vivo photothermal cancer therapy of HA-MoS_2 conjugates. a) Antitumor effect of HA-MoS_2 conjugates determined by MTT assay after incubation for 2 h without and with NIR laser illumination for 10 min. The control data were obtained after incubation for 24 h (**$p < 0.01$). b) Relative tumor volume (V/V_0) with increasing time for 9 days (**$p < 0.01$, HA-MoS_2 conjugates with NIR laser illumination vs the others). (inset) A photo-image showing the antitumor effect of PTT by the injection of HA-MoS_2 conjugates with and without NIR laser illumination. c–f) Histological TUNEL assay of tumor tissues after treatment of (c) PBS, (d) PBS with NIR laser illumination, (e) HA-MoS_2 conjugates, and (f) HA-MoS_2 conjugates with NIR laser illumination (scale bar = 100 μm). g) Histological analysis with H&E staining of dissected lung, liver, spleen, and kidney after intravenous injection of HA-MoS_2 conjugates (scale bar = 500 μm).

various concentrations of MoS_2 under NIR laser illumination (**Figure 6**a). In case of cells treated without NIR laser illumination, there was no critical antitumor effect up to the concentration of 200 μg mL^{-1}. In addition, when the cells were exposed to only NIR laser without incubation with HA-MoS_2 conjugates, the cell viability did not decrease significantly. However, in case of cells incubated with HA-MoS_2 conjugates for 2 h, the antitumor effect was drastically enhanced with increasing concentration by NIR laser illumination. The viability of HCT116 cells significantly decreased above 100 μg mL^{-1} of HA-MoS_2 conjugate concentrations when illuminated by NIR laser. These results confirmed the photothermal effect of HA-MoS_2 conjugates on cancer cells.

After that, in vivo cancer PTT was performed in tumor-bearing mice. PBS as a control and 100 μg mL^{-1} of HA-MoS_2 conjugates were injected into the tumor site at both sides of flank. Then, only one side was illuminated with NIR laser for 10 min (see inset of Figure 6b). By measuring the tumor volume, we could clearly confirm the photothermal effect of HA-MoS_2 conjugates with NIR laser illumination on the tumor region. The group of PBS, PBS+NIR, and HA-MoS_2 conjugates without NIR laser illumination did not show any significant tumor ablation effect. However, after photothermal ablation of the tumor with HA-MoS_2 conjugates and NIR laser illumination, there was no further tumor growth and relapse in comparison to the continuous tumor growth of other groups (Figure 6b). To investigate the tumor apoptosis induced by the photothermal ablation, dissected tumor tissues were analyzed by TUNEL assay (Figure 6c–f). The TUNEL positive area was stained green and nuclei of normal cells were stained blue. Although no significant apoptosis was observed in the tumor region after treatment with PBS, PBS+NIR, and HA-MoS_2

conjugates without NIR laser illumination, the tumor tissues treated with HA-MoS_2 conjugates and NIR laser showed the significantly effective apoptosis of tumor cells (Figure 6f). Finally, to further assess in vivo safety of HA-MoS_2 conjugates, we carried out histological analysis of dissected organs including lung, liver, spleen, and kidney (Figure 6g). There were no inflammation and histological difference after treatment with PBS and HA-MoS_2 conjugate, revealing the physiological safety of HA-MoS_2 conjugates.

Taken together, we could confirm the feasibility of HA-MoS_2 conjugates for further multimodal cancer theranosis. For example, small chemical drugs can be loaded to the MoS_2 surface of HA-MoS_2 conjugates by π–π staking and hydrophobic interaction.[45,46]

Due to the high surface-to-volume ratio, MoS_2 might be served as a suitable drug carrier platform with high efficiency. It would be a noble approach to chemically and photothermally treat various cancer cells, such as MDA-MB-231 (human breast adenocarcinoma), Hela (human epithelioid cervix carcinoma), and B16F10 (musculus skin melanoma) cells.[29,45] In addition, the lower cytotoxicity of exfoliated MoS_2 was reported than that of graphene and its analogues.[47] Furthermore, the upconversion property of HA-MoS_2 conjugates might be exploited for various applications to photomedicine in the deep tissue.[48] These are inspiring features of HA-MoS_2 conjugates for biomedical applications, enabling multimodal imaging and multimodal therapy of various cancer diseases. With more studies on the fundamental scientific background, HA-MoS_2 conjugate might open a new way to the futuristic multifunctional cancer theranosis.

3. Conclusions

Multifunctional HA-MoS_2 conjugates were successfully developed for multimodal bioimaging and PTT of cancers. MoS_2 nanoparticle could be easily surface modified with thiolated HA by simple mixing to enhance the biocompatibility, physiological stability, and tumor targeting efficiency. HA-MoS_2 conjugate showed the unique optical properties of upconversion and downconversion for fluorescence imaging and further applications to photomedicine. Noticeably, HA-MoS_2 conjugate appeared to be in situ cleaved in the reducing environment, enhancing the fluorescence signal and the photothermal effect. Using continuous and pulsed NIR, in vivo PAT and PTT were also effectively performed for the treatment of tumor-bearing mice. We believe our facile system of MoS_2 conjugated with HA can be successfully developed as a novel multifunctional theranostic nanoplatform for multimodal imaging and multimodal therapy of various cancer diseases.

4. Experimental Section

Exfoliation of MoS_2: Dispersed MoS_2 nanomaterials were prepared using the simple aqueous exfoliation method as described elsewhere.[21] Briefly, 90 mg of bulk MoS_2 powder was dispersed in 30 mL of NMP, which was ultrasonicated (VCX750, Sonics Inc.) for 3 h. Then, the dispersion was transferred to a serum bottle and kept at 140 °C with vigorous stirring for 6 h. Afterwards, the suspension was centrifuged (1248R, Labogene) at 3000 rpm for 15 min. Finally, the brownish yellow supernatant containing MoS_2 was dialyzed using a cellulose membrane (MWCO = 3 kDa) against DI water for 2 days.

Preparation and Characterization of HA-MoS_2 and PEG-MoS_2 Conjugates: HA-SH was synthesized by the conjugation of cystamine to activated carboxyl group of HA with 1-ethyl-3-(3-dimethylaminopropyl) carbodiimide (EDC) and the following reduction with dithiothreitol (DTT).[20] HA-SH (1 mg mL^{-1}) was added to MoS_2 (4 mg mL^{-1}) in DI water, which was sonicated for 20 min. After that, the mixed solution was stirred overnight for the disulfide bond formation. PEG-MoS_2 conjugates were prepared using thiolated PEG (PEG-SH, MW = 10 kDa) as reported elsewhere.[13] After stirring, the mixture was filtered with a PD10 desalting column to remove the unreacted MoS_2. The hydrodynamic size and Zeta-potential were measured by DLS (Zetasizer Nano, Malvern Instrument Co., UK). The chemical structure was analyzed by FT-IR (Nicolet 6700 FT-IR spectrometer, Thermo Fisher Sciengific Co., Waltham, MA). The UV–vis and PL spectra were obtained with a UV transilluminator (DUT-260, Core Bio System, Korea) and a fluorescence spectrometer (FP-6500, JASCO, Japan). The particle size and morphology were observed with an AFM (VEECO Instrument, New York, NY), a TEM (JEM-1011, JEOL, Japan), and an HR-TEM (JEM-2200FS with Cs-corrected TEM, JEOL, Japan). The binding energy spectrum was obtained by XPS (ESCA LAB250, VG scientific). Each sample for AFM and XPS analysis was prepared by drop casting of 0.1 mL solution on the clean silicon wafer. The sample placed wafer was dried in vacuum overnight. After that, the remaining solution was removed with a nitrogen air-gun.

Fluorescence Bioimaging of HA-MoS_2 Conjugates: Multicolor cellular imaging was performed using HCT116 cells seeded on an 8-chamber glass slide at a density of 2×10^4 cells per well for 24 h and cultured for 24 h. After that, the media were exchanged with serum-free media containing 40 μg mL^{-1} of HA-MoS_2 conjugates. The cells were incubated for 2 h, washed with PBS, fixed with 4% paraformaldehyde solution at room temperature for 10 min, washed again with PBS, and mounted with Vectashield mounting medium (Vector Laboratories, Inc., Burlingame, CA). Then, the cells were visualized with a confocal laser scanning microscope (Leica CM 1850 cryostat, Leica, Deerfield, IL) at different filter wavelengths of 415–480 nm, 496–563 nm, 570–637 nm, and 642–709 nm.

In vivo biodistribution of HA-MoS_2 conjugates was investigated to assess the tumor targeting affinity and the fluorescence imaging feasibility of HA-MoS_2 conjugates. Female mice inoculated with HCT116 cells on the dorsal skin were randomly divided into three groups and treated with: 1) PBS as a negative control, 2) PEG-MoS_2 conjugates as a positive control, and 3) HA-MoS_2 conjugates. All mice were fully anesthetized by intraperitoneal injection of a combination of ketamine (100 mg kg^{-1}) and xylazine (10 mg kg^{-1}). All mice were equally treated by the injection of 0.1 mL each sample at a concentration of 40 μg mL^{-1} to the jugular vein. At 4 h post-injection, all animals were sacrificed, and their lungs, livers, spleens, kidneys, and tumors were carefully dissected and washed with PBS for quantitative fluorescence imaging for the ROI using an IVIS imaging system (IVIS Spectrum) at an excitation wavelength of 465 nm and an emission wavelength filter of 520 nm, respectively. The relative fluorescence intensity of each organ was normalized to the total sum of the fluorescence in the organs. After ex vivo imaging, all organs were fixed in 4% formalin, embedded in paraffin, sectioned, H&E stained, and visualized by optical imaging microscopy (Olympus BX51M, Olympus, UK). The POSTECH institutional ethical protocols for animals were followed.

In Vitro Monitoring of Disulfide Cleavage in the Reducing Environment: The synthesized HA-MoS_2 conjugates were treated with TCEP at the same molar ratio of HA. After incubation for 24 h, the hydrodynamic diameter and Zeta-potential were measured by DLS. In addition, in vitro photothermal effect on the solution temperature change was assessed with and without TCEP treatment under NIR light illumination for 10 min. HiLyte647 dye was conjugated to HA chain as a fluorescent indicator for the intracellular monitoring of disulfide cleavage. In brief, HA-MoS_2 conjugates were mixed with 2 M excess of EDC and 4 mol% of HiLyte647 amine. After stirring for 2 h, the solution was dialyzed against 0.3 N NaCl aqueous solution and DI water to remove the remaining

EDC and the unreacted HiLyte647 amine. HiLyte647 was visualized by the confocal microscopy at the excitation and emission wavelengths of 649 and 674 nm, and MoS_2 at the wavelengths of 416 and 480 nm, respectively. The receptor-mediated endocytosis of HA-MoS_2 conjugates was assessed by HA preincubation test with confocal microscopic imaging using HCT116 and B16F10 cells with HA receptors, and HEK293 cells without HA receptors. These cells were preincubated with 4 M excess of HA for 2 h before the treatment with HA-MoS_2 conjugates. After fixation and mounting with DAPI (Vector Laboratories, Inc., Burlingame, CA), the cells were visualized by confocal microscopy at the wavelength of 390 and 496 nm.

Photoacoustic Imaging of HA-MoS_2 Conjugates: In vitro and in vivo PA images were obtained using acoustic-resolution reflection-mode PA imaging system. A Q-switched Nd:YAG laser (SLII-10; Continuum) at 532 nm wavelength was used for pumping a tunable OPO laser (Surelite OPOPLIS; Continuum), which provided a 5 ns pulse duration over the wavelength tuning range of 680–2500 nm at a 10 Hz repetition rate. To avoid PA signal generation from the surface, the illuminated laser beam had a donut-shaped pattern achieved by passing through a conical lens and an optical condenser. The pulsed laser energy was ≈5 mJ cm^{-2}. In vitro PA signals of both MoS_2 and HA-MoS_2 conjugates at the same optical density at 750 nm were measured from 680 to 950 nm. Each signal was normalized to the power of each laser. The wavelengths of 680 and 850 nm were used for in vivo PA imaging. The same methods and animal models were used for in vivo PTT described in the following section. A spherically focused ultrasonic transducer with a 5 MHz center frequency (V308; Olympus NDT) was applied for detecting the generated PA signals. A pulser/receiver (5072PR, Olympus NDT) and a digital oscilloscope (MSO 5204; Tektronix) were used for amplifying the PA signal and recoding, respectively. Two linear scanners were used to perform raster scanning to obtain volumetric PA imaging. As described above, female mice inoculated with HCT116 cells on the dorsal skin were treated by the injection of PBS or HA-MoS_2 conjugates. To improve the acoustic coupling efficiency, the mouse was put into a homemade water tank containing an ultrasound gel. The 5 MHz ultrasonic transducer induced axial and lateral resolutions of 145 and 950 µm, respectively. It took ≈30 min to acquire one 3D PA image.

Photothermal Ablation of HA-MoS_2 Conjugates: Using Dulbecco's modified Eagle medium (DMEM) supplemented with 10 vol% of FBS and 1 vol% of antibiotics, HCT116 cells were seeded on 96-well plates at a density of 6×10^3 cells per well in an incubator with 5% CO_2 atmosphere at 37 °C for 24 h. Then, HA-MoS_2 conjugates were dissolved in each cell medium at various concentrations from 0 to 200 µg mL^{-1} for 24 h. The antitumor effect of HA-MoS_2 conjugates was assessed by the standard MTT assay. The optical density was measured at 540 nm with a microplate reader (EMax microplate reader, Bucher Biotec AG, Basel, Switzerland). All photothermal ablation tests were performed using 808 nm NIR laser with a power density of 1 W cm^{-2}. In order for in vivo cancer PTT, HCT116 cells at a density of 5×10^6 in 100 µL were subcutaneously inoculated into both sides of dorsal skin of female BALB/c nude mice. After tumor growth to an average volume of 47.37 mm^3 for 10 days, 100 µL of PBS or HA-MoS_2 conjugates (100 µg mL^{-1}) was intratumorally injected to the mice. Before injection, each mouse was fully anesthetized by intraperitoneal injection of a combination of ketamine (100 mg kg^{-1}) and xylazine (10 mg kg^{-1}). Then, the tumor site on each group was treated with or without NIR illumination for 10 min. A relative tumor volume was monitored using the following equation: tumor volume = $A \times B^2/2$ (A: maximum, B: minimum diameter of the tumor) and each tumor volume was divided by its original one. After 12 h, the photo-image of NIR light–treated region was taken with a digital camera (Samsung, Seoul, Korea), and all tumor sites were excised and fixed in 4% formaldehyde solution over 3 days for further histological and apoptosis analyses with TUNEL assay.

Statistical Analysis: Statistical analysis was performed via the *t*-test using the software of SigmaPlot10.0 (Systat Software Inc. San Jose, CA). Data were expressed as means ± standard deviation (SD) from several separate experiments. All experiments were done at least three times ($n = 3$). Figure 6b was analyzed by ANOVA test using the same software. The values for $*p < 0.05$ and $**p < 0.01$ were considered statistically significant.

Supporting Information

Supporting Information is available from the Wiley Online Library or from the author.

Acknowledgements

This research was supported by the Center for Advanced Soft-Electronics (Global Frontier Project, CASE-2015M3A6A5072945), Nano·Material Technology Development Program (No. 2017M3A7B8065278), Global Ph.D. Fellowship Program (2015H1A2A1034046) and Basic Science Research Program (2017R1E1A1A03070458) of the National Research Foundation (NRF) funded by the Ministry of Science and ICT, Republic of Korea. This work was also supported by the World Class 300 Project (S2482887) funded by the Ministry of SMEs and Startups, Republic of Korea.

Conflict of Interest

The authors declare no conflict of interest.

Keywords

hyaluronate, intracellular reduction, molybdenum disulfide, multi-functional theranosis, tumor targeting

Received: August 22, 2018
Revised: October 29, 2018
Published online: November 27, 2018

[1] H. Y. Lee, Z. Li, K. Chen, A. R. Hsu, C. Xu, J. Xie, S. Sun, X. Chen, *J. Nucl. Med.* **2008**, *49*, 1371.
[2] H. Lee, M.-Y. Lee, S. H. Bhang, B. S. Kim, Y. S. Kim, J. H. Ju, K. S. Kim, S. K. Hahn, *ACS Nano* **2014**, *8*, 4790.
[3] W. J. Rieter, J. S. Kim, K. M. L. Taylor, H. An, W. Lin, T. Tarrant, W. Lin, *Angew. Chem., Int. Ed.* **2007**, *46*, 3680.
[4] L. Cheng, K. Yang, Y. Li, J. Chen, C. Wang, M. Shao, S. T. Lee, Z. Liu, *Angew. Chem., Int. Ed.* **2011**, *50*, 7385.
[5] J. S. Kim, W. J. Rieter, K. M. L. Taylor, H. An, W. Lin, W. Lin, *J. Am. Chem. Soc.* **2007**, *129*, 8962.
[6] D. Lee, H. Koo, I. Sun, J. H. Ryu, K. Kim, I. C. Kwon, *Chem. Soc. Rev.* **2012**, *41*, 2656.
[7] L. Cheng, J. Liu, X. Gu, H. Gong, X. Shi, T. Liu, C. Wang, X. Wang, G. Liu, H. Xing, W. Bu, B. Sun, Z. Liu, *Adv. Mater.* **2014**, *26*, 1886.
[8] T. Liu, S. Shi, C. Liang, S. Shen, L. Cheng, C. Wang, X. Song, S. Goel, T. E. Barnhart, W. Cai, Z. Liu, *ACS Nano* **2015**, *9*, 950.
[9] A. Jawaid, K. Park, M. Jespersen, A. Qualley, P. Mirau, L. F. Drummy, R. A. Vaia, *Chem. Mater.* **2016**, *28*, 337.
[10] R. Kurapati, K. Kostarelos, M. Prato, A. Bianco, *Adv. Mater.* **2016**, *28*, 6052.
[11] S. S. Chou, B. Kaehr, J. Kim, B. M. Foley, M. De, P. E. Hopkins, J. Huang, C. J. Brinker, V. P. Dravid, *Angew. Chem., Int. Ed.* **2013**, *52*, 4160.
[12] S. K. C., R. C. Longo, R. Addou, R. M. Wallace, K. Cho, *Nanotechnology* **2014**, *25*, 375703.
[13] C. Ataca, H. Şahin, S. Ciraci, *J. Phys. Chem. C* **2012**, *116*, 8983.
[14] C. H. Park, H. Yang, J. Lee, B. J. Kim, *Adv. Funct. Mater.* **2017**, *27*, 1604403.

[15] W. Feng, L. Chen, M. Qin, X. Zhou, Q. Zhang, Y. Miao, K. Qiu, Y. Zhang, C. He, *Sci. Rep.* **2015**, *5*, 17422.
[16] S. Wang, Y. Chen, X. Li, W. Gao, L. Zhang, J. Liu, Y. Zheng, H. Chen, J. Shi, *Adv. Mater.* **2015**, *27*, 7117.
[17] S. Wang, K. Li, Y. Chen, H. Chen, M. Ma, J. Feng, Q. Zhao, J. Shi, *Biomaterials* **2015**, *39*, 206.
[18] J. Li, W. Yin, L. Yan, J. Yu, G. Tian, L. Zhou, X. Zheng, X. Zhang, Y. Yong, J. Li, Z. Gu, Y. Zhao, *ACS Nano* **2014**, *7*, 6922.
[19] S. Wang, X. Li, Y. Chen, X. Cai, H. Yao, W. Gao, Y. Zheng, X. An, J. Shi, H. Chen, *Adv. Mater.* **2015**, *27*, 2778.
[20] K. Yang, H. Xu, L. Cheng, C. Sun, J. Wang, Z. Liu, *Adv. Mater.* **2012**, *24*, 5586.
[21] J. Wang, R. Yan, F. Guo, M. Yu, F. Tan, *Nanotechnology* **2016**, *27*, 285102.
[22] J. Kim, H. Kim, W. J. Kim, *Small* **2016**, *12*, 1184.
[23] E. J. Oh, K. Park, S. K. Kim, J. Yang, J. Kong, M. Young, A. S. Hoffman, S. K. Hahn, *J. Controlled Release* **2010**, *141*, 2.
[24] L. A. Johnson, S. Banerji, W. Lawrance, U. Gileadi, G. Prota, K. A. Holder, Y. M. Roshorm, T. Hanke, V. Cerundolo, N. W. Gale, D. G. Jackson, *Nat. Immunol.* **2017**, *18*, 762.
[25] H. Wen, C. Dong, H. Dong, A. Shen, W. Xia, X. Cai, Y. Song, X. Li, Y. Li, D. Shi, *Small* **2012**, *8*, 760.
[26] L. Udabage, G. R. Brownlee, S. K. Nilsson, T. J. Brown, *Exp. Cell Res.* **2005**, *310*, 205.
[27] S. Xu, D. Li, P. Wu, *Adv. Funct. Mater.* **2015**, *25*, 1127.
[28] H. S. Jung, W. H. Kong, D. K. Sung, M. Lee, S. E. Beack, D. H. Keum, K. S. Kim, S. H. Yun, S. K. Hahn, *ACS Nano* **2014**, *8*, 260.
[29] T. Wang, H. Zhu, J. Zhuo, Z. Zhu, P. Papakonstantinou, G. Lubarsky, J. Lin, M. Li, *Anal. Chem.* **2013**, *85*, 10289.
[30] M. Jeong, S. Kim, S. Ju, *RSC Adv.* **2016**, *6*, 36248.
[31] Q. Ji, Y. Zhang, T. Gao, Y. Zhang, M. Liu, Y. Chen, X. Qiao, P. Tan, M. Kan, J. Feng, Q. Sun, Z. Liu, *Nano Lett.* **2013**, *13*, 3870.
[32] H. Dong, S. Tang, Y. Hao, H. Yu, W. Dai, G. Zhao, Y. Cao, H. Lu, X. Zhang, H. Ju, *ACS Appl. Mater. Interfaces* **2016**, *8*, 3107.
[33] Y. Chen, W. Frey, S. Kim, P. Kruizinga, K. Homan, S. Emelianov, *Nano Lett.* **2011**, *11*, 348.
[34] L. Cheng, C. Wang, Z. Liu, *Nanoscale* **2013**, *5*, 23.
[35] J. Nam, N. Won, H. Jin, H. Chung, S. Kim, *J. Am. Chem. Soc.* **2009**, *131*, 13639.
[36] W. W. Yu, L. Qu, W. Guo, X. Peng, *Chem. Mater.* **2003**, *15*, 2854.
[37] I. Moreels, K. Lambert, D. De Muynck, F. Vanhaecke, D. Poelman, J. C. Martins, G. Allan, Z. Hens, *Chem. Mater.* **2007**, *19*, 6101.
[38] P. K. Jain, K. S. Lee, I. H. El-sayed, M. A. El-sayed, *J. Phys. Chem. B* **2006**, *110*, 7238.
[39] E. J. Goh, K. S. Kim, Y. R Kim, H. S. Jung, S. Beack, W. H. Kong, G. Scarcelli, S. H. Yun, S. K. Hahn, *Biomacromolecules* **2012**, *13*, 2554.
[40] A. Mero, M. Campisi, *Polymers* **2014**, *6*, 346.
[41] J. V. Jokerst, A. J. Cole, V. D. D. Sompel, S. S. Gambhir, *ACS Nano* **2012**, *6*, 10366.
[42] W. Li, P. Rong, K. Yang, P. Huang, K. Sun, X. Chen, *Biomaterials* **2015**, *45*, 18.
[43] M. Lee, C. Lee, H. S. Jung, M. Jeon, K. S. Kim, S. H. Yun, C. Kim, S. K. Hahn, *ACS Nano* **2016**, *10*, 822.
[44] C. Lee, W. Kwon, S. Beack, D. Lee, Y. Park, H. Kim, K. Hahn, S. Rhee, C. Kim, *Theranostics* **2016**, *6*, 2196.
[45] T. Liu, C. Wang, X. Gu, H. Gong, L. Cheng, X. Shi, L. Feng, B. Sun, Z. Liu, *Adv. Mater.* **2014**, *26*, 3433.
[46] J. Zhao, P. Xie, C. Ye, C. Wu, W. Han, M. Huang, S. Wang, H. Chen, *Chem. Eng. J.* **2018**, *351*, 157.
[47] W. Z. Teo, E. L. K. Chng, Z. Sofer, M. Pumera, *Chem. - Eur. J.* **2014**, *20*, 9627.
[48] S. Nizamoglu, M. C. Gather, M. Humar, M. Choi, S. Kim, K. S. Kim, S. K. Hahn, G. Scarcelli, M. Randolph, R. W. Redmond, S. H. Yun, *Nat. Commun.* **2016**, *7*, 10374.